JACS
JOURNAL OF THE AMERICAN CHEMICAL SOCIETY

Article

pubs.acs.org/JACS

Ultrasensitive Nanosensors Based on Upconversion Nanoparticles for Selective Hypoxia Imaging in Vivo upon Near-Infrared Excitation

Jianan Liu,[†,#] Yong Liu,[‡,#] Wenbo Bu,*[,†] Jiwen Bu,[§] Yong Sun,[‡] Jiulin Du,[§] and Jianlin Shi*[,†]

[†]State Key Laboratory of High Performance Ceramics and Superfine Microstructure, Shanghai Institute of Ceramics, Chinese Academy of Sciences, 1295 Ding-xi Road, Shanghai 200050, PR China

[‡]Cancer Research Institute, Fudan University Shanghai Cancer Hospital, Fudan University, Shanghai 200032, PR China

[§]Institute of Neuroscience and State Key Laboratory of Neuroscience, Shanghai Institutes for Biological Sciences, Chinese Academy of Sciences, 320 Yue-Yang Road, Shanghai 200031, PR China

Supporting Information

ABSTRACT: Hypoxia is a distinct feature of malignant solid tumors, which is a possible causative factor for the serious resistance to chemo- and radiotherapy or the development of invasion and metastasis. The exploration of nanosensors with the capabilities like the accurate diagnosis of hypoxic level will be helpful to estimate the malignant degree of tumor and subsequently implement more effective personalized treatment. Here, we report the design and synthesis of nanosensors that can selectively and reversibly detect the level of hypoxia both in vitro and in vivo. The designed nanosensor is composed of two main moieties: oxygen indicator $[Ru(dpp)_3]^{2+}Cl_2$ for detection of hypoxia and upconversion nanoparticles for offering the excitation light of $[Ru(dpp)_3]^{2+}Cl_2$ by upconversion process under 980 nm exposure. The results show that the nanosensors can reversibly become quenched or luminescent under hyperoxic or hypoxic conditions, respectively. Compared with free $[Ru(dpp)_3]^{2+}Cl_2$, the designed nanosensors exhibit enhanced sensitivity for the detection of oxygen in hypoxic regions. More attractively, the nanosensors can image hypoxic regions with high penetration depth because the absorption and emission wavelength are within the NIR and far-red region, respectively. Most importantly, nanosensors display a high selectivity for detection of relevant oxygen changes in cells and zebrafish.

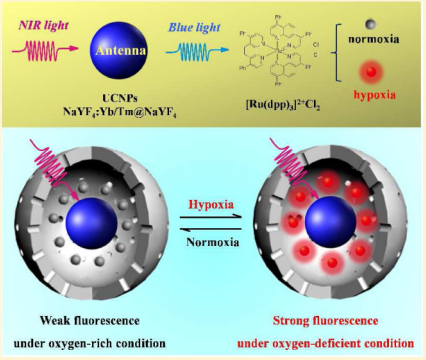

INTRODUCTION

Hypoxia is a distinct feature of various diseases including tumors,[1] cardiovascular diseases,[2] and stroke.[3] In solid tumors, hypoxia is mainly caused by inadequate tumor blood flow due to the enhanced tumor proliferative activity and the abnormal structure of tumor vessels. In some hypoxic regions, the oxygen concentration can be as low as 0%.[4] Hypoxic human tumors have been shown to be not only resistant to radiotherapy, chemotherapy and other treatment modalities, but also much more biologically aggressive, more likely to recur locally and metastasize than "normal" tumors.[5−7] Therefore, highly sensitive and selective detection of tumor hypoxia are vitally important and necessary to guide the subsequent treatments.[8,9]

Currently available approaches to detect hypoxic regions, such as positron emission tomography (PET)[10] and magnetic resonance imaging,[11] face the challenges of radioactive risk and inaccurate diagnosis, respectively. Fortunately, optical imaging remains to be the most attractive approach because it offers various advantages including high sensitivity and simplicity.[12,13] Very recently, several hypoxia-sensitive fluorescence probes, whose fluorescence intensity will change under the bioreductive microenvironment of hypoxia, have been developed by employing nitro group,[14,15] quinone group,[16] azo group[17−19] or QSY-21[20] as the hypoxia-sensing moieties. However, these examples of hypoxia-sensitive fluorescent probes suffer from two drawbacks that will hinder their potential biomedical applications.

First, such indirect sensing methodologies of hypoxia were mediated by the redox reactions caused by the reductive microenvironment of hypoxia. However, thiol compounds[21] such as glutathione (GSH),[22,23] widely existing in cancer cells, are also the cellular reducing agents that can contribute to a reductive environment. Therefore, the observed signal changes in redox reactions cannot be exclusively attributed to the hypoxia. Hence, the development of optical sensors which can selectively and quantitatively assess oxygen concentration in vitro and in vivo is highly desirable.

Second, most of available hypoxia-sensitive fluorescent probes require the excitation of high-energy ultraviolet (UV) or visible light, neither of which can penetrate into hypoxic regions buried deeply in tumors and both of which can cause detrimental effect to healthy cells and organs. To overcome this problem, one effective way is to utilize hypoxia-sensing systems that can be directly excited by near-infrared (NIR) light that exhibit the properties of remarkably less biological damaging and deeper tissue penetration.[24−27] However, the reported organic dyes-based NIR fluorescent probes are always subject

Received: April 29, 2014
Published: June 23, 2014

dx.doi.org/10.1021/ja5042989 | J. Am. Chem. Soc. 2014, 136, 9701−9709

to the low photostability and quantum yield in bioenvironment.[28]

A better alternative strategy to harvest the NIR light is to use antennae species that absorb NIR light and transfer the harvested energy to the light with specific wavelength, which can be used as excitation light of the highly efficient hypoxia indicators. Recently, lanthanide-doped upconversion nanoparticles (UCNPs) have received considerable attention because they can not only emit upconverted UV, visible, and NIR light[29,30] with high photostability[31] and show deep tissue-penetration depths (up to 10 mm)[32] under NIR (980 nm) exposure, but also be used as antenna that up-convert NIR light into the necessary light to excite the photoresponsive agents via a LRET (upconversion luminescence resonance energy transfer) process.[33−36] Fortunately, in order to detect oxygen molecules under NIR excitation,[37] great efforts have been made, and recent years have witnessed the successful exploration of UCNPs-based sensors that integrate UCNPs and oxygen indicator into one system, in the forms of thin films[38] or UCNP core/dense silica shell nanoparticles.[39] However, all of these sensors are limited to detecting oxygen in extracellular environments due to the insufficient sensitivity and large sizes of film materials. Therefore, the development of a nanosized UCNPs-based nanosensor that can probe the oxygen molecules in both cells and even living organisms with high enough sensitivity and high selectivity is still challenging.

In the study described below, we report on a novel design of LRET nanosensor containing two moieties: UCNP core/hollow mesoporous silica shell-structured nanoparticles and oxygen indicator tris (4, 7-diphenyl-1,10-phenanthroline) ruthenium(II) dichloride (designated as $[Ru(dpp)_3]^{2+}Cl_2$). The developed nanosensors possess several special characteristics: (i) upon NIR exposure, the upconverted visible light emitted by UCNPs can be used as donor for $[Ru(dpp)_3]^{2+}Cl_2$, and the results show that the nanosensors can reversibly become quenched or illuminated alternatively under hyperoxic or hypoxic conditions both in living cells and zebrafish with a high signal-to-noise ratio; (ii) compared with free $[Ru(dpp)_3]^{2+}Cl_2$, the designed nanosensors exhibit substantially enhanced sensitivity for the detection of oxygen in hypoxic regions; (iii) the more important is the high selectivity and specificity for the detection of oxygen changes by the nanosensors, which is unaffected by acidic and reducing microenvironment such as natural thiol compounds in cancer cells. To the best of our knowledge, such a nanosensor is the first probe that can selectively detect hypoxia degree both in vitro and in vivo under NIR excitation with high sensitivity.

EXPERIMENTAL SECTION

Adsorption of $[Ru(dpp)_3]^{2+}Cl_2$ on the Hollow Cavity of UCNP@hmSiO$_2$. $[Ru(dpp)_3]^{2+}Cl_2$ (5 mg) was dissolved in PBS (10 mL). UCNP@hmSiO$_2$ (50 mg) was added to the solution, and the suspension was protected from light and stirred at room temperature for 24 h. The as-prepared nanosensor was collected by centrifugation at 13000 r/min for 15 min. After centrifugation, the sample was washed with PBS for four times. The amount of adsorbed $[Ru(dpp)_3]^{2+}Cl_2$ was determined from the difference between the starting amount of $[Ru(dpp)_3]^{2+}Cl_2$ and the amount of the supernatant liquid measured by UV−vis at a wavelength of 463 nm. The loading amount of $[Ru(dpp)_3]^{2+}Cl_2$ on UCNP@hmSiO$_2$ was calculated as follows: $(M_{initial} - M_{remain})/(M_{initial} - M_{remain} + M_{UCNP@hmSiO_2})$.

Hypoxic Conditions for Live Cell Luminescent Imaging. O_2 concentration in the range of 1−20% was controlled with a multi gas incubator (Sanyo) by means of N_2 substitution.

Luminescent Observation of Hypoxic Degree in U87MG Cells and Zebrafish by Confocal Laser Scanning Microscopy (CLSM) Imaging. For CLSM observations, U87MG cells (10^5 cells per dish) were seeded in coverglass bottom dishes (35 mm × 10 mm) under normoxic (20% pO_2) conditions, and then treated with nanosensors at the concentration of 500 μg/mL. After the incubation for 12 h, the media were removed, and the cells were then washed twice with D-Hank's solution to remove the residual nanosensors. Subsequently, the cells were treated with fresh media. Then, the cells were incubated under various conditions (1, 5, 10, 15, 20% pO_2) for 6 h. After that, the cells were visualized under a confocal laser scanning microscope (FluoView FV1000, Olympus) in the real time. The fluorescence images were taken under 100× oil-immersion objective. For different incubation conditions (various oxygen concentrations), the same parameters were used for all CLSM images. For HeLa cells, same procedures were performed with U87MG cells except different cell lines used.

As control experiments, the hypoxic and normoxic cancer cells were treated with α-lipoic acid (LPA, 500 μM) for 24 h. Then, the cell lines were washed for three times with cell culture media and incubated with nanosensors (500 μg/mL) for another 6 h. Finally, the cell lines were further washed using cell culture media and subsequently imaged.

For in vivo CLSM images, zebrafish embryos were microinjected with nanosensors (500 μg/mL), and then superfused with 15 mM 2,3-Butanedione (BDM), which will result in the cerebral anoxia. Five minutes later, zebrafish was visualized under a CLSM in the real time. The fluorescence images were taken under 10× water-immersion objective. The parameters used here were same with in vitro experiments.

RESULTS AND DISCUSSION

Design and Principle of the Nanosensors for the Detection of Cellular Oxygen. Our design strategy is based on the fact that UCNPs can be used as energy donors for the LRET process but themselves have no oxygen recognition capability. $[Ru(dpp)_3]^{2+}Cl_2$ was chosen as the quenchable indicator for sensing oxygen because its maximum absorbance located at 463 nm strongly overlaps with the two emission wavelengths (at 450 and 475 nm) of UCNPs (Figure 1), while $[Ru(dpp)_3]^{2+}Cl_2$ cannot be directly photoexcited by NIR light. More importantly, the red luminescence of $[Ru(dpp)_3]^{2+}Cl_2$ at 613 nm can be strongly quenched by oxygen (Figure S1, Supporting Information),[40] and has no overlap with the emission of the UCNPs. Thus, it is expected that the red emission of $[Ru(dpp)_3]^{2+}Cl_2$ at 613 nm could be modulated by

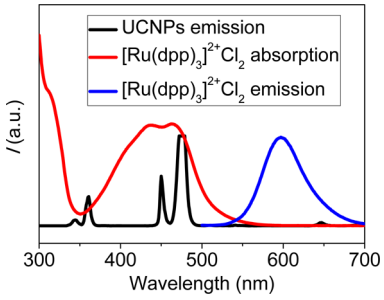

Figure 1. Normalized absorption and emission spectra showing the spectral overlap of the emission of the $NaYF_4$:Yb/Tm nanoparticles with the absorption of the oxygen probe $[Ru(dpp)_3]^{2+}Cl_2$. Black line: emission spectrum of the nanoparticles under photoexcitation at 980 nm. Red and blue line: absorbance and emission spectrum of $[Ru(dpp)_3]^{2+}Cl_2$, respectively.

dx.doi.org/10.1021/ja5042989 | J. Am. Chem. Soc. 2014, 136, 9701−9709

Scheme 1. Schematic Illustration of the Structure of Nanosensors and Their Sensing to Oxygen with a Change in Luminescence Emission

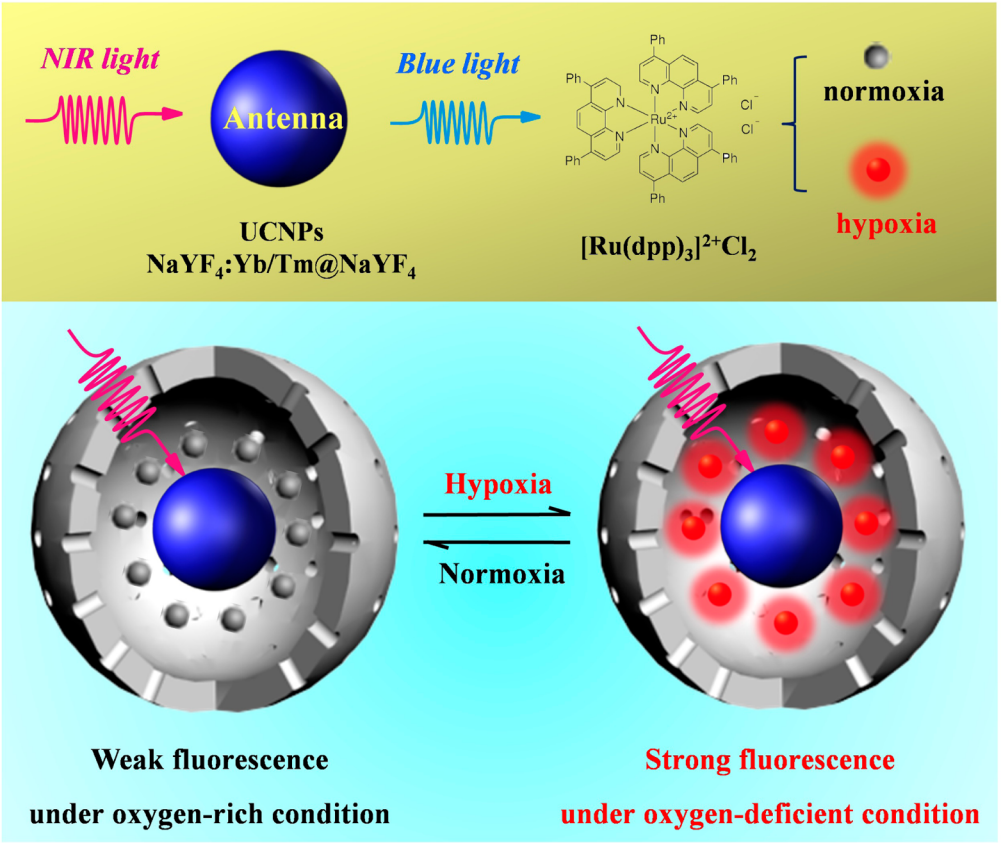

the presence/absence or concentration of oxygen species when under the excitation by the upconverted blue emissions at 450 and 475 nm of UCNPs under external NIR exposure. It is worth noting that both the external excitation and the red emission (980 nm/613 nm) are within the "optical window" of the biological tissues,[41] which will enable deep tissue imaging.[42] As shown in Scheme 1, in order to combine UCNPs and $[Ru(dpp)_3]^{2+}Cl_2$ into one system, a composite UCNP core/hollow mesoporous silica shell (UCNP@hmSiO$_2$) nanostructure is constructed, and then $[Ru(dpp)_3]^{2+}Cl_2$ is encapsulated into the hollow cavity to ensure the LRET occurrence between UCNPs and $[Ru(dpp)_3]^{2+}Cl_2$ efficiently. Therefore, the resulted core–shell nanostructure (designated as nanosensors) will provide promising opportunity for the real-time monitoring of oxygen level in biological applications.

Synthesis and Characterization of UCNP@hmSiO$_2$. The preparation details of UCNP@hmSiO$_2$ are described as follows. First, the $NaYF_4$:Yb/Tm@$NaYF_4$ UCNPs core with the diameters of 33 nm (Figure S2, Supporting Information) was obtained by thermal decomposition method.[43] Compared with $NaYF_4$:Yb/Tm, $NaYF_4$:Yb/Tm@$NaYF_4$ displayed a strong enhancement in the upconverted luminescence (UCL) intensity upon excitation at the wavelength of 980 nm (Figure S3, Supporting Information). Then a layer of dense silica of ~10 nm in thickness was coated on the surface of UCNPs (denoted as UCNP@dSiO$_2$) in the reverse-micelle solution containing Igepal CO-520 and cyclohexane.[44] Mesoporous silica shells were further coated onto the UCNP@dSiO$_2$ (denoted as UCNP@dSiO$_2$@mSiO$_2$) in aqueous solution containing hexadecyl trimethylammonium chloride (CTAC) under basic conditions.[45] Finally, rattle-structured UCNP@hmSiO$_2$ were obtained by etching dense silica layer in hot water (95 °C) via "surface-protected etching" process.[46] Scanning electron microscopy (SEM) and scanning transmission electron microscopy (STEM) images (Figure 2a–c, Figure S4, Supporting Information) indicate that UCNP@dSiO$_2$, UCNP@dSiO$_2$@mSiO$_2$, and UCNP@hmSiO$_2$ were successfully fabricated step-by-step. They exhibit uniform morphology with excellent dispersity, which was also confirmed by dynamic light scattering (DLS) analysis (Figure S5, Supporting Information). We further utilized high angle annular dark field STEM (HAADF-STEM) to analyze the element distributions in UCNP@hmSiO$_2$. The results (Figure 2d) show that fluorine (F) and silicon (Si) elements are distributed in the UCNP core and mesoporous silica shell, respectively. The formation of hollow structure was also confirmed by nitrogen adsorption–desorption isotherms (Figure S6 and Table S1, Supporting Information), which show that compared with UCNP@dSiO$_2$@mSiO$_2$, UCNP@hmSiO$_2$ possessed a relatively high pore volume of 1.15 cm^3g^{-1} with a Brunauer–Emmett–Teller (BET) surface area of 567.4 $m^2\ g^{-1}$ and a pore size distribution of 4.4 nm. Such a large hollow cavity is especially beneficial to the energy transfer between UCNPs and $[Ru(dpp)_3]^{2+}Cl_2$ because each UCNP's surface is closely surrounded and attached by sufficient amount of $[Ru(dpp)_3]^{2+}Cl_2$, and the distance between the donors and acceptors is ensured to be within 10 nm.

$[Ru(dpp)_3]^{2+}Cl_2$ loading is based on the electrostatic attraction between the oppositely charged species since the zeta potential of $[Ru(dpp)_3]^{2+}Cl_2$ and UCNP@hmSiO$_2$ was

dx.doi.org/10.1021/ja5042989 | J. Am. Chem. Soc. 2014, 136, 9701–9709

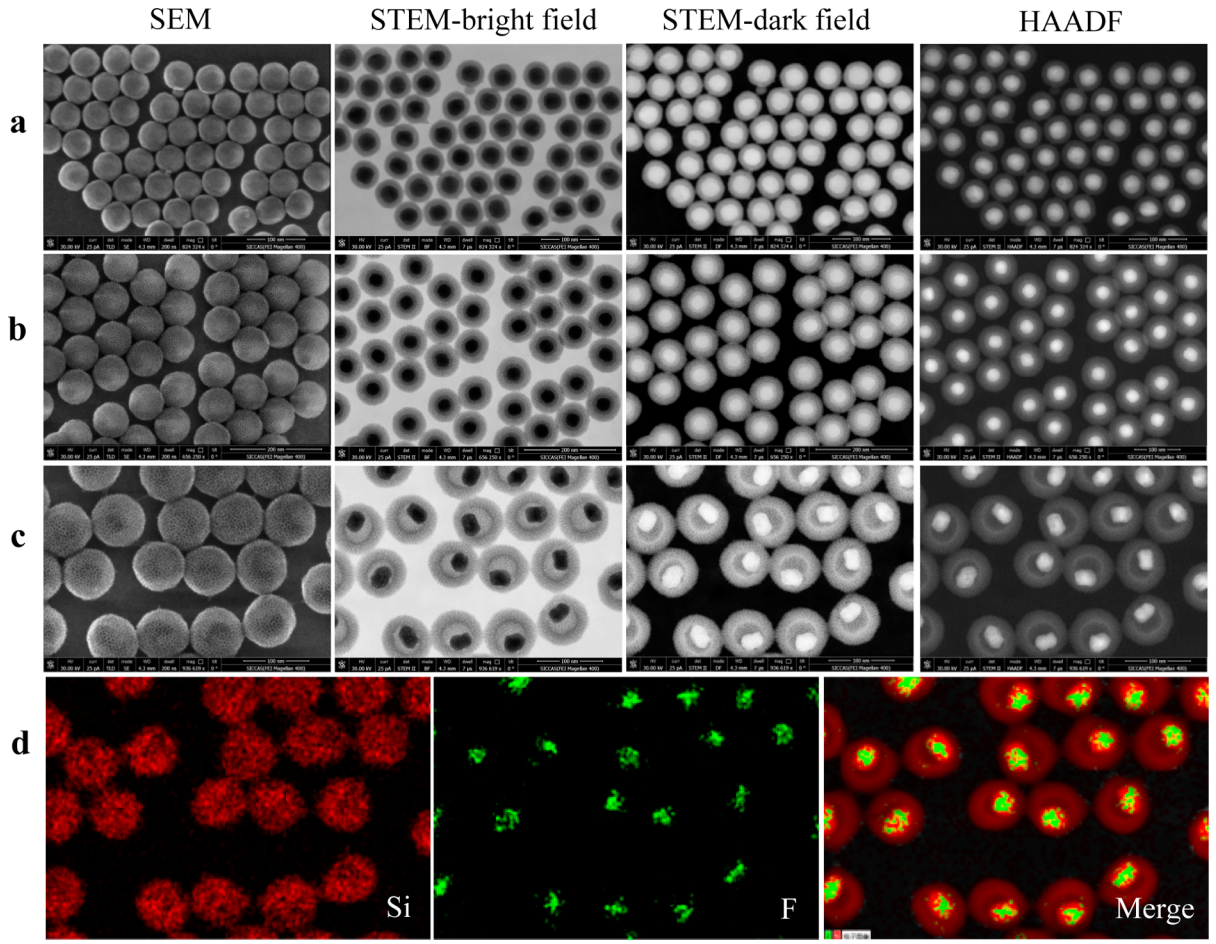

Figure 2. Scanning electron microscopy (SEM), bright/dark field scanning transmission electron microscopy (STEM), and high angle annular dark field (HAADF) images of UCNP@dSiO$_2$ (a), UCNP@dSiO$_2$@mSiO$_2$ (b), and UCNP@hmSiO$_2$ (c). (d) Corresponding elemental (F, Si) mappings of UCNP@hmSiO$_2$.

+43.8 and −41.6 mV, respectively (Figure S7, Supporting Information). The successful loading of $[Ru(dpp)_3]^{2+}Cl_2$ into the UCNP@hmSiO$_2$ was confirmed by FTIR spectra (Figure S8, Supporting Information). By measuring the absorbance at 463 nm with the UV−vis absorbance technique, the loading amount of $[Ru(dpp)_3]^{2+}Cl_2$ in UCNP@hmSiO$_2$ was determined to be 6.7 wt %. This result is similar to that obtained by inductively coupled plasma optical emission spectrometer (ICP-OES), which indicates a 3.26 unit of $[Ru(dpp)_3]^{2+}Cl_2$ per luminescence center (Tm^{3+}). In addition, the nanoparticles after loading $[Ru(dpp)_3]^{2+}Cl_2$ are stable in aqueous solutions or cell culture media for at least three months without visible aggregation or sedimentation if kept at 4 °C in the dark.

LRET Efficiency. We next assessed the optical properties of the nanosensors. UV−vis absorption spectroscopy showed an intense and broad band centered at 463 nm, which is a characteristic of $[Ru(dpp)_3]^{2+}Cl_2$ (Figure S9, Supporting Information). Figure 3a shows the emission spectra of the UCNP@hmSiO$_2$ dispersed in aqueous solution before and after loading $[Ru(dpp)_3]^{2+}Cl_2$ under excitation at 980 nm. After loading $[Ru(dpp)_3]^{2+}Cl_2$, the intensities of the emission bands of UCNP@hmSiO$_2$ that peaked at 450 and 477 nm are significantly reduced, because the strong absorption by $[Ru(dpp)_3]^{2+}Cl_2$ via LRET. This energy transfer is further confirmed by the appearance of the luminescence of the probe $[Ru(dpp)_3]^{2+}Cl_2$, indicating that the oxygen indicator has been photoexcited by the blue emissions from the UCNPs. In this LRET process, which is considered to be nonradiative,[47,48] the excitation of UCNPs (donor) by NIR light (980 nm) triggers an energy transfer to $[Ru(dpp)_3]^{2+}Cl_2$ (acceptor) and the acceptor in turn emits light at its characteristic wavelength since they are located close to each other within 10 nm and show spectrally overlapped donor emission and acceptor absorption. The LRET efficiency was measured to be ∼90.1%, as deduced from the upconversion emission spectra of the nanosensor. In sharp contrast, a simple physical mixing of UCNP@hmSiO$_2$ and $[Ru(dpp)_3]^{2+}Cl_2$ only led to a 0.03-fold decrease in the UCL emission at 450 and 477 nm (Figure S10, Supporting Information). These results confirm that the quenching effect of UCL emission in the nanosensors should be mainly ascribed to the LRET process rather than a simple light absorption process by $[Ru(dpp)_3]^{2+}Cl_2$. Moreover, in the nanosensors without hollow structure, relatively insignificant quenching in the UCL emission was measured with a LRET efficiency of ∼27% (Figure S11, Supporting Information). These facts evidence that the hollow structure in the nanosensors plays an important role in intensifying LRET and consequently enhancing the LRET efficiency. The quantum efficiency of UCNP@hmSiO$_2$, defined as the ratio of photons emitted to photons absorbed,[49] was determined to be 0.35% upon 980 nm NIR laser excitation at a power density of 150 W cm^{-2}. Though the value is significantly lower than that of other luminescent

dx.doi.org/10.1021/ja5042989 | J. Am. Chem. Soc. 2014, 136, 9701−9709

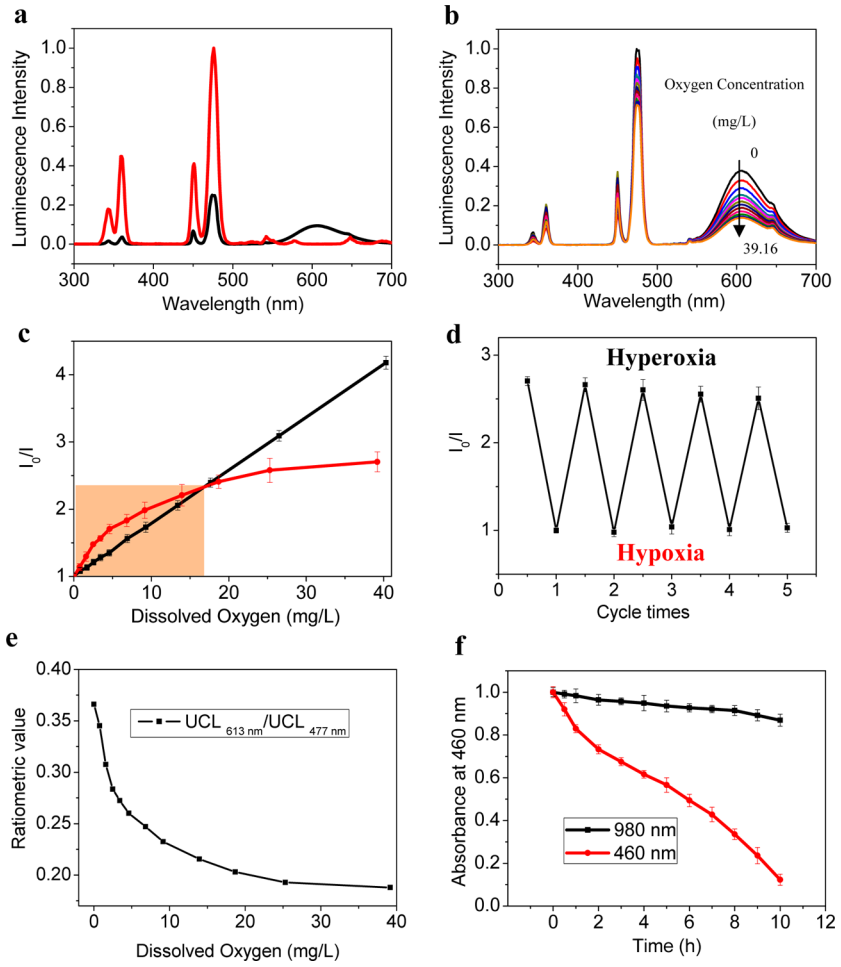

Figure 3. (a) Upconversion emission spectra of UCNP@hmSiO$_2$ before (red line) and after (black line) loading $[Ru(dpp)_3]^{2+}Cl_2$. (b) Oxygen-dependent UCL spectra of nanosensors at varied concentrations of dissolved oxygen. (c) Respective calibration plots of free $[Ru(dpp)_3]^{2+}Cl_2$ (black line) and nanosensors (red line) at different concentrations of dissolved oxygen. $[Ru(dpp)_3]^{2+}Cl_2$ was excited by 460 nm light, while the nanosensors were excited by 980 nm light. (d) Luminescent emission responses of nanosensor to hypoxia−hyperoxia cycles. (e) The intensity ratio of the UCL emission of at 613 to 477 nm as a function of dissolved oxygen concentration. (f) Photostability of nanosensor under the continuous illumination by 980 nm laser (0.5 W cm^{-2}) and 460 nm lamp (0.1 W cm^{-2}) for 10 h.

nanoparticles, such as quantum dots[50] and dye-doped nanoparticles,[51] UCNPs-based nanosensors still attract extensive attention due to the unique features of a long lifetime, high photochemical stability and reduced photobleaching.

Selective Sensing of the Oxygen by Nanosensors. We next tested oxygen detection capability in aqueous solutions using such a nanosensor. Figure 3b shows the real-time sensor's responses to various concentrations of oxygen. The red emission (maximized at 613 nm) of the designed nanosensor is strongly quenched by the introduction of sufficient oxygen. There is a poly exponential relationship (Figure 3c) between the dissolved oxygen concentration and the intensity ratio I_0/I (where I_0 is the luminescence intensity of nanosensor in oxygen-free solution, and I is the one in solutions of various concentrations of O_2). The ratio of the luminescence intensities in oxygen-free and in oxygen-saturated solution is as high as 2.6, which means that the nanosensors are highly sensitive to oxygen. Compared to free $[Ru(dpp)_3]^{2+}Cl_2$ under blue 460 nm excitation, the nanosensors show enhanced sensitivity in relatively low oxygen pressure (less than 15 mg/L) under NIR 980 nm excitation. This makes the nanosensors a useful probe for the sensing and imaging of oxygen concentration in biological applications. In addition, all signal changes are fully reversible as shown in Figure 3d. The reversible hypoxia cycle could be repeated for at least 5 times with only a modest fluorescence decrement (7.4% was bleached during the process). All the above results reveal that the designed nanosensor is a high-performance reporter that, through LRET, can be used to quantitatively measure the amount of oxygen using NIR excitaion.

It is widely accepted that compared to fluorescent intensity-based sensing approach, ratiometric sensing is an especially reliable method that can quantify the detected object more precisely.[52] In this case of UCNP-based nanosensors, ratiometric sensing also becomes possible due to the existence of two emission bands (477/613 nm) of the nanosensors, one of which (613 nm) is more greatly influenced by the oxygen than the other (477 nm). Hence, the intensity ratio of UCL between at 613 and 477 nm, i.e., $UCL_{613\ nm}/UCL_{477\ nm}$, was chosen as the detection signals. As the oxygen concentrations increase, the UCL ratio ($UCL_{613\ nm}/UCL_{477\ nm}$) gradually decrease (Figure 3e), indicating that the nanosensors are capable of serving as a potential probe for ratiometric UCL detection of oxygen.

The properties of high selectivity and photostability are very important for an excellent nanosensor. Attractively, the

dx.doi.org/10.1021/ja5042989 | J. Am. Chem. Soc. 2014, 136, 9701−9709

chemical response of $[Ru(dpp)_3]^{2+}Cl_2$ is highly selective toward oxygen relative to other biomolecules. The investigation reveals that acidic and reducing microenvironment did not lead to noticeably optical responses (Figure S12, Supporting Information), implying that the nanosensor selectively reacts with physiological levels of oxygen in a concentration-dependent manner. Furthermore, the photostabilities of nanosensors under the illumination of 980 and 460 nm light were investigated. Under continuous irradiation using a 980 nm laser or 460 nm lamp with a power density of 0.5 or 0.1 W cm^{-2} for 10 h, the absorbance of nanosensors at 463 nm decreased by 13.1 and 87.7%, respectively (Figure 3f). Therefore, using UCL emission as the excitation light for $[Ru(dpp)_3]^{2+}Cl_2$, the nanosensor showed remarkably improved photostability, which can be more useful in practical applications.

Mechanistic Studies. More experiments were conducted to investigate the mechanism of sensitivity enhancement of nanosensors over free $[Ru(dpp)_3]^{2+}Cl_2$. We first prepared three kinds of materials: vacuum-freeze-dried UCNP@$dSiO_2$, UCNP@$dSiO_2$@$mSiO_2$, and UCNP@$hmSiO_2$, and then they were introduced into the water solution (20 mL) with the dissolve oxygen concentration of 10 mg/L. As shown in Figure 4a, compared to UCNP@$dSiO_2$, UCNP@$dSiO_2$@$mSiO_2$ has

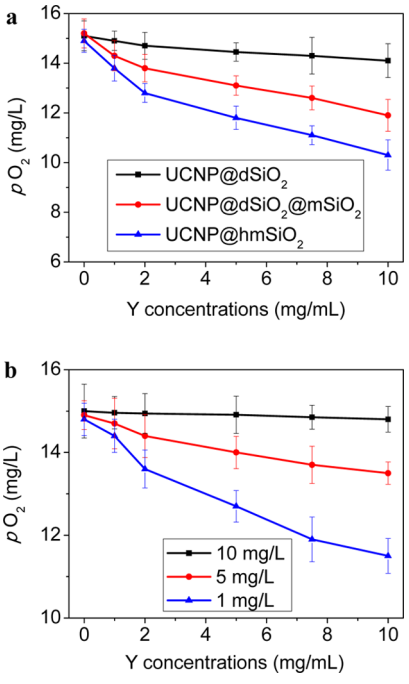

Figure 4. (a) The variation of oxygen concentration in water solutions after the introduction of vacuum-freeze-dried UCNP@$dSiO_2$, UCNP@$dSiO_2$@$mSiO_2$, and UCNP@$hmSiO_2$. (b) The variation of oxygen concentration in water solutions after the introduction of centrifuged UCNP@$hmSiO_2$, which has been predispersed in water solutions of varied oxygen concentrations (1, 5, and 10 mg/L).

led to obvious decrease of oxygen concentration in solutions, indicating that small oxygen molecules can be adsorbed strongly into mesopores, which is in line with a previous report.[53] More importantly, significant decrease of oxygen concentration was observed after introducing UCNP@$hmSiO_2$. The above observations clearly suggest that both mesoporous silica shell and hollow cavity in nanosensors can contribute to the adsorption of oxygen molecules from solutions, resulting in the local oxygen enrichment; i.e., the local concentrations of oxygen molecules in the nanosensors will be significantly higher than those in solution matrix under hypoxic conditions. Such an enhanced oxygen adsorption effect of the nanosensors makes it possible to detect low concentrations of oxygen with high sensitivity and is also advantageous for the potential clinical detection of hypoxic degree.

To gain insight into the adsorption capability under the different conditions of hypoxia or hyperoxia, studies were carried out as follows. Vacuum-freeze-dried UCNP@$hmSiO_2$ nanoparticles were predispersed in solutions of varied oxygen concentrations (1, 5, and 10 mg/L). Afterward, they were centrifuged and directly added into another water solution of a fixed oxygen concentration of 15 mg/L. When UCNP@$hmSiO_2$ was predispersed in a solution of the oxygen concentrations of 10 mg/L, no significant change of oxygen concentration was found (Figure 4b). In comparison, when predispersed in solutions of the lower oxygen concentrations of 1 and 5 mg/L, clear decreases in oxygen concentration was observed. These results indicate that the adsorption process of oxygen can no longer occur when oxygen concentrations are higher than 10 mg/L since the adsorption of oxygen has been saturated under this condition. The local oxygen concentrations in the nanosensors will depend on the adsorption/diffusion efficiency of oxygen into the porous network when oxygen concentrations are below or above 10 mg/L. Thus, the sensitivity of the nanosensors can vary significantly from hypoxia to hyperoxia conditions. This may explain the observed nonlinear response of the nanosensors between hypoxia and hyperoxia conditions.

Sensing Hypoxia in Living Cells. Since the nanosensors show high oxygen sensitivity, selectivity, and reversibility with respect to the hypoxia environment, we next applied the nanosensors to detect hypoxia in living cells and investigated whether they could distinguish oxygen concentrations inside living cells under physiological conditions. We chose the U87MG cell line as a bioassay model because head and neck tumors are more prone to be hypoxic, and the malignant glioma typically exhibits a necrosis core and the surrounding areas of chronic hypoxia.[54] To evaluate the cytotoxicity of the nanosensors, we performed a standard 3-(4,5-dimethylthiazol-2-yl)-2,5-diphenyltetrazolium bromide (MTT) assay on both the hypoxic and normoxic U87MG cells with nanosensor concentrations from 15.6 to 500 μg/mL. The results clearly demonstrate that the nanosensor is of low toxicity toward cultured cell lines under the experimental conditions at the concentration of as high as 500 μg/mL (Figure S13, Supporting Information). The nanosensors were incubated with U87MG cancer cells under normoxia conditions for 12 h. After removing the unuptaken nanosensors and subsequently adding fresh cell-culture media, the cells were incubated under decreased oxygen concentrations (e.g., 20, 15, 10, 5, 1% O_2) for 6 h. This treatment induced significant increase in the expression of HIF-1α (Figure S14, Supporting Information), indicating the appearance of hypoxia in the cells. Subsequently, cells were examined by confocal laser scanning microscopy (CLSM) imaging. In this experiment, strong luminescent intensity was detected from the cells incubated at low oxygen concentrations (e.g., 1 and 5%) (Figure 5). In sharp contrast, U87MG cells treated with nanosensors under normoxic conditions (e.g., 20% oxygen concentration) show negligible intracellular fluorescence. As control experiments, we observed that luminescent intensity did not change (Figure S15,

dx.doi.org/10.1021/ja5042989 | J. Am. Chem. Soc. 2014, 136, 9701−9709

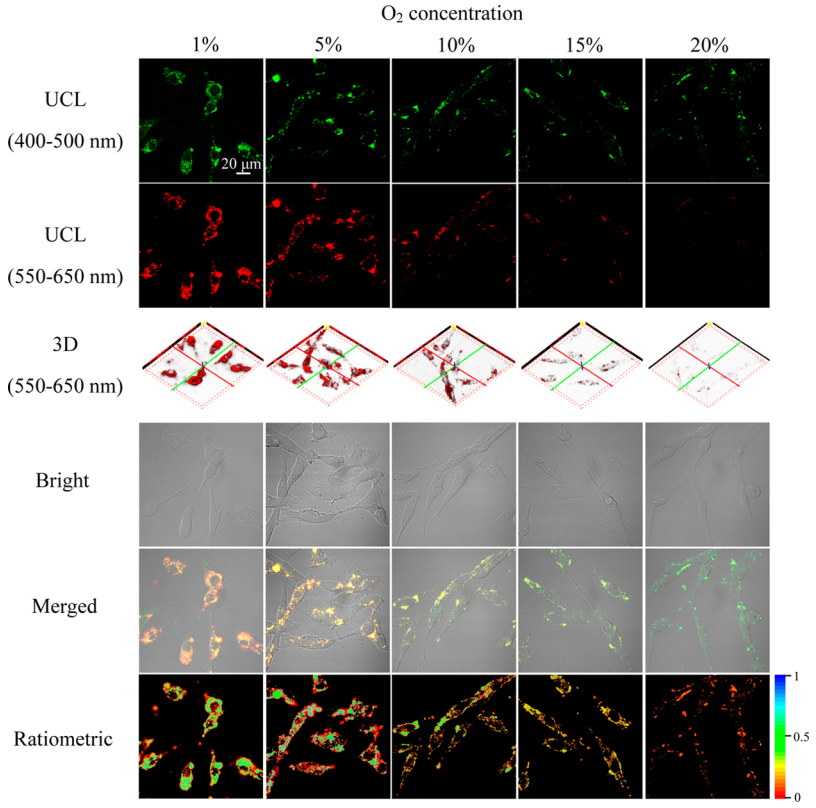

Figure 5. Oxygen-dependent UCL (400−500 nm and 550−650 nm) decrease of nanosensors inside living U87MG cells. Ratiometric UCL images ($UCL_{550-650\ nm}/UCL_{400-500\ nm}$) were also shown. Confocal laser scanning microscopy (CLSM) image of nanosensors loaded U87MG cells incubated under varied oxygen levels. All images have the same scale bar (20 μm). λ_{ex} = 980 nm; λ_{em} = 400−500 nm/550−650 nm.

Supporting Information) for hypoxia or normoxic U87MG cancer cells pretreated with α-lipoic acid (LPA, a GSH synthesis enhancer:[55] 500 μM). These results indicate that the changes in luminescent intensity of nanosensors occur only when they are bound to oxygen molecules, and the reductive microenvironment does not affect the measurements of intracellular oxygen levels. We also examined another cell line (HeLa) and obtained similar data (Figure S16 and S17, Supporting Information). Hence, it can be concluded that the nanosensors are capable of visualizing the hypoxic status in varied cell lines via the detection of luminescent intensity.

Furthermore, on the basis of the rapid decrease of UCL ratio ($UCL_{613\ nm}/UCL_{477\ nm}$) of the nanosensors when interacted with oxygen molecules, the ratiometric UCL imaging in vitro was further investigated. The UCL ratio of the red channel (λ_{UCL} = 550−650 nm) to blue channel (λ_{UCL} = 400−500 nm) was used as the detecting signal. As shown in Figure 5, hypoxic U87MG cells incubated with nanosensors show a UCL ratio of 0.2. In contrast, incubation of normoxic U87MG cells with nanosensors result in a higher UCL ratio of 0.4. These results suggest that the designed nanosensors could be used for probing hypoxic degree in vitro with the ratiometric UCL method.

Next, we investigated whether this nanosensor can reversibly detect repeated cycles of hypoxia-normoxia in living cells. Cycles of hypoxia−normoxia were established by alternatively incubating U87MG cells at 20% and 1% oxygen environment repeatedly. As expected, weak fluorescence can be observed under normoxia (Figure 6a). After incubation at hypoxia condition for another 6 h, the red emission intensity in the cells dramatically increases (Figure 6b). The same changes of

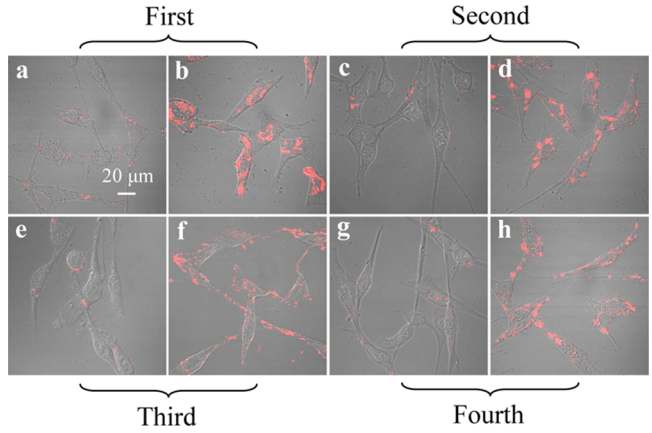

Figure 6. CLSM images of U87MG cells loaded with nanosensors and exposed to cycles of normoxia−hypoxia. (a) Cells were incubated under normoxia for 6 h in DMEM containing nanosensors, then washed with PBS (pH 7.4), and placed in fresh DMEM. (b) The cells were incubated under hypoxic condition for 6 h after (a). (c−h) Subsequently, the cells were incubated under normoxia (c,e,g) and hypoxia (d,f,h) conditions for 6 h. Such process was repeated up to four times. All images have the same scale bar (20 μm). λ_{ex} = 980 nm; λ_{em} = 550−650 nm.

luminescent intensity of the cells were observed when the normoxia−hypoxia cycle was repeated three times (Figure 6c−h). As a control, no fluorescence intensity change was observed when cells were incubated under normoxia for at least 24 h (Figure S18, Supporting Information). Taken together, the data show that this nanosensor can report multiple hypoxia−normoxia cycles by a reversible optical response in living cells.

dx.doi.org/10.1021/ja5042989 | J. Am. Chem. Soc. 2014, 136, 9701−9709

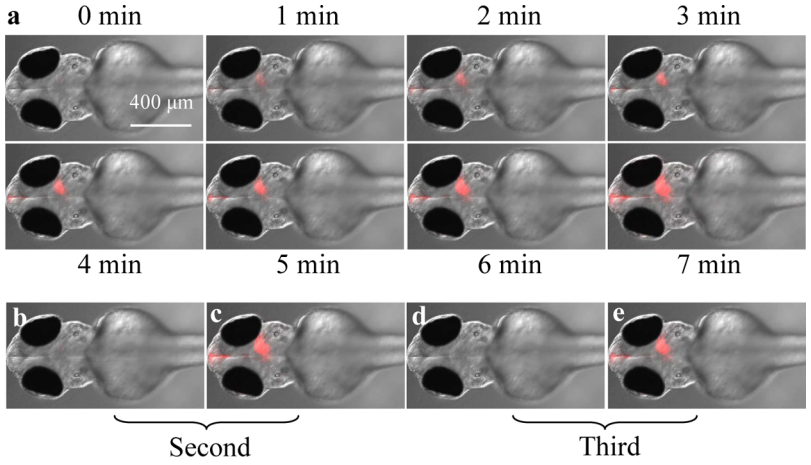

Figure 7. (a) CLSM images of living zebrafish embryos after injection of nanosensors followed by adding BDM as described in the text. UCL images were obtained for 28 min, under the excitation at 980 nm and emission at 550−650 nm. (b) After adding fresh water, red emission in the brain was quenched under NIR exposure. (c−e) Such process can be repeated for three times. All images have the same scale bar (400 μm).

Sensing Hypoxia in Vivo. Encouraged by the satisfactory response characteristics of the nanosensors in vitro, we examined whether such nanosensors can detect hypoxia in the intact animal in vivo using a cerebral anoxia model of the zebrafish. It has been demonstrated that incubation of zebrafish embryos with 15 mM 2,3-butanedione (BDM) can completely abolish cardiac contractility, which results in the cerebral anoxia.[56] In addition, the effects of BDM on contractility can be reversed after BDM washout. When a solution of nanosensors (500 μg/mL) was administered to zebrafish embryos' brain by intracerebral microinjection, no luminescence can be observed. In 5 min after the introduction of BDM, the luminescent intensity in the brain rapidly increased due to cerebral anoxia, and after another 7 min, the luminescent intensity was saturated (Figure 7a and Movie S1, Supporting Information). In contrast, after the introduction of fresh water, the luminescent intensity significantly decreased owing to the recovery of oxygen concentration (Figure 7b and Movie S2, Supporting Information). As expected, the injection of a second aliquot of BDM resulted in another decrease of oxygen stress and an increase in cerebral luminescence. This luminescent quenching and recovery along with normoxic and hypoxic conditions can be reversible for at least three times (Figure 7c−e). These results indicate that the developed nanosensor can be a useful tool to reversibly detect hypoxia not only in living cells, but also in living animals.

CONCLUSIONS

In summary, we have performed a comprehensive study of a UCNPs-based nanosensor and successfully demonstrated their use as biosensors in the NIR-excited detections of oxygen levels reversibly both in vitro and in vivo. The nanosensor reacts with oxygen selectively and in a concentration-dependent manner. In addition, based on the LRET mechanism by using $[Ru(dpp)_3]^{2+}Cl_2$ as acceptors and UCNPs as donors respectively with long wavelength red emission and NIR excitation, the interference by the strong luminescence background in living organisms can be well-suppressed. Importantly, they can be utilized for imaging oxygen gradients within live tumor cells, as well as for probing oxygen in zebrafish microenvironments. We anticipate that this nanosensor will be a valuable platform for sensing the level of hypoxia in solid tumors, which is essential to guide the subsequent therapeutic decisions. Furthermore, on the basis of the above principle, such an approach presented here can be used broadly in the fundamental research of NIR luminescent nanosensors for biologically imaging gas component, pH value, temperature variation, or specific ions.

ASSOCIATED CONTENT

Supporting Information

Detailed experimental procedures for the synthesis and characterizations of the nanosensors, control experiments in vitro and in vivo. This material is available free of charge via the Internet at http://pubs.acs.org.

AUTHOR INFORMATION

Corresponding Authors

wbbu@mail.sic.ac.cn
jlshi@mail.sic.ac.cn

Author Contributions

#J.L. and Y.L. contributed equally to this work.

Notes

The authors declare no competing financial interest.

ACKNOWLEDGMENTS

This work has been financially supported by the National Natural Science Foundation of China (Grant No. 51372260, 51132009), the Shanghai Rising-Star Program (Grant No. 12QH1402500), the Nano special program of the Science and Technology Commission of Shanghai (Grant No. 11 nm0505000), the Shanghai Yangfan Program (Grant No. 14YF1406400), and the Shanghai Pujiang Program (Grant No. 13PJ1401600).

REFERENCES

(1) Wilson, W. R.; Hay, M. P. *Nat. Rev. Cancer* **2011**, *11*, 393.
(2) Garvey, J. F.; Taylor, C. T.; McNicholas, W. T. *Eur. Respir. J.* **2009**, *33*, 1195.
(3) Prass, K.; Scharff, A.; Ruscher, K.; Löwl, D.; Muselmann, C.; Victorov, I.; Kapinya, K.; Dirnagl, U.; Meisel, A. *Stroke* **2003**, *34*, 1981.
(4) Vaupel, P.; Schlenger, K.; Knoop, C.; Hockel, M. *Cancer Res.* **1991**, *51*, 3316.
(5) Harris, A. L. *Nat. Rev. Cancer* **2002**, *2*, 38.
(6) Brown, J. M.; Wilson, W. R. *Nat. Rev. Cancer* **2004**, *4*, 437.

(7) Facciabene, A.; Peng, X.; Hagemann, I. S.; Balint, K.; Barchetti, A.; Wang, L.-P.; Gimotty, P. A.; Gilks, C. B.; Lal, P.; Zhang, L.; Coukos, G. *Nature* **2011**, *475*, 226.
(8) Vaupel, P.; Mayer, A. *Cancer Metastasis Rev.* **2007**, *26*, 225.
(9) Lee, N.; Cho, H. R.; Oh, M. H.; Lee, S. H.; Kim, K.; Kim, B. H.; Shin, K.; Ahn, T.-Y.; Choi, J. W.; Kim, Y.-W.; Choi, S. H.; Hyeon, T. *J. Am. Chem. Soc.* **2012**, *134*, 10309.
(10) Fujibayashi, Y.; Taniuchi, H.; Yonekura, Y.; Ohtani, H.; Konishi, J.; Yokoyama, A. *J. Nucl. Med.* **1997**, *38*, 1155.
(11) Iwaki, S.; Hanaoka, K.; Piao, W.; Komatsu, T.; Ueno, T.; Terai, T.; Nagano, T. *Bioorg. Med. Chem. Lett.* **2012**, *22*, 2798.
(12) Zhang, G.; Palmer, G. M.; Dewhirst, M. W.; Fraser, C. L. *Nat. Mater.* **2009**, *8*, 747.
(13) Zhang, S.; Hosaka, M.; Yoshihara, T.; Negishi, K.; Iida, Y.; Tobita, S.; Takeuchi, T. *Cancer Res.* **2010**, *70*, 4490.
(14) Cui, L.; Zhong, Y.; Zhu, W.; Xu, Y.; Du, Q.; Wang, X.; Qian, X.; Xiao, Y. *Org. Lett.* **2011**, *13*, 928.
(15) Nakata, E.; Yukimachi, Y.; Kariyazono, H.; Im, S.; Abe, C.; Uto, Y.; Maezawa, H.; Hashimoto, T.; Okamoto, Y.; Hori, H. *Bioorg. Med. Chem.* **2009**, *17*, 6952.
(16) Komatsu, H.; Harada, H.; Tanabe, K.; Hiraoka, M.; Nishimoto, S.-i. *Med. Chem. Comm.* **2010**, *1*, 50.
(17) Kiyose, K.; Hanaoka, K.; Oushiki, D.; Nakamura, T.; Kajimura, M.; Suematsu, M.; Nishimatsu, H.; Yamane, T.; Terai, T.; Hirata, Y.; Nagano, T. *J. Am. Chem. Soc.* **2010**, *132*, 15846.
(18) Piao, W.; Tsuda, S.; Tanaka, Y.; Maeda, S.; Liu, F.; Takahashi, S.; Kushida, Y.; Komatsu, T.; Ueno, T.; Terai, T.; Nakazawa, T.; Uchiyama, M.; Morokuma, K.; Nagano, T.; Hanaoka, K. *Angew. Chem., Int. Ed.* **2013**, *52*, 13028.
(19) Perche, F.; Biswas, S.; Wang, T.; Zhu, L.; Torchilin, V. P. *Angew. Chem., Int. Ed.* **2014**, *53*, 3362.
(20) Takahashi, S.; Piao, W.; Matsumura, Y.; Komatsu, T.; Ueno, T.; Terai, T.; Kamachi, T.; Kohno, M.; Nagano, T.; Hanaoka, K. *J. Am. Chem. Soc.* **2012**, *134*, 19588.
(21) Sen, C. K. *Biochem. Pharmacol.* **1998**, *55*, 1747.
(22) Lee, M. H.; Yang, Z.; Lim, C. W.; Lee, Y. H.; Dongbang, S.; Kang, C.; Kim, J. S. *Chem. Rev.* **2013**, *113*, 5071.
(23) Deng, R.; Xie, X.; Vendrell, M.; Chang, Y.-T.; Liu, X. *J. Am. Chem. Soc.* **2011**, *133*, 20168.
(24) Xu, K.; Wang, F.; Pan, X.; Liu, R.; Ma, J.; Kong, F.; Tang, B. *Chem. Commun.* **2013**, *49*, 2554.
(25) Guo, T.; Cui, L.; Shen, J.; Zhu, W.; Xu, Y.; Qian, X. *Chem. Commun.* **2013**, *49*, 10820.
(26) Okuda, K.; Okabe, Y.; Kadonosono, T.; Ueno, T.; Youssif, B. G. M.; Kizaka-Kondoh, S.; Nagasawa, H. *Bioconjugate Chem.* **2012**, *23*, 324.
(27) McLaurin, E. J.; Greytak, A. B.; Bawendi, M. G.; Nocera, D. G. *J. Am. Chem. Soc.* **2009**, *131*, 12994.
(28) Gonçalves, M. S. T. *Chem. Rev.* **2009**, *109*, 190.
(29) Wang, F.; Liu, X. *Acc. Chem. Res.* **2014**, *47*, 1378.
(30) Gorris, H. H.; Wolfbeis, O. S. *Angew. Chem., Int. Ed.* **2013**, *52*, 3584.
(31) Park, Y. I.; Kim, J. H.; Lee, K. T.; Jeon, K. S.; Bin Na, H.; Yu, J. H.; Kim, H. M.; Lee, N.; Choi, S. H.; Baik, S. I.; Kim, H.; Park, S. P.; Park, B. J.; Kim, Y. W.; Lee, S. H.; Yoon, S. Y.; Song, I. C.; Moon, W. K.; Suh, Y. D.; Hyeon, T. *Adv. Mater.* **2009**, *21*, 4467.
(32) Zhou, J.; Liu, Z.; Li, F. Y. *Chem. Soc. Rev.* **2012**, *41*, 1323.
(33) Park, Y. I.; Kim, H. M.; Kim, J. H.; Moon, K. C.; Yoo, B.; Lee, K. T.; Lee, N.; Choi, Y.; Park, W.; Ling, D.; Na, K.; Moon, W. K.; Choi, S. H.; Park, H. S.; Yoon, S.-Y.; Suh, Y. D.; Lee, S. H.; Hyeon, T. *Adv. Mater.* **2012**, *24*, 5755.
(34) Huang, P.; Zheng, W.; Zhou, S.; Tu, D.; Chen, Z.; Zhu, H.; Li, R.; Ma, E.; Huang, M.; Chen, X. *Angew. Chem., Int. Ed.* **2014**, *53*, 1252.
(35) Liu, Y.; Chen, M.; Cao, T.; Sun, Y.; Li, C.; Liu, Q.; Yang, T.; Yao, L.; Feng, W.; Li, F. *J. Am. Chem. Soc.* **2013**, *135*, 9869.
(36) Mader, H. S.; Wolfbeis, O. S. *Anal. Chem.* **2010**, *82*, 5002.
(37) Wang, X.-d.; Wolfbeis, O. S. *Chem. Soc. Rev.* **2014**, *43*, 3666.
(38) Achatz, D. E.; Meier, R. J.; Fischer, L. H.; Wolfbeis, O. S. *Angew. Chem., Int. Ed.* **2011**, *50*, 260.
(39) Liu, L.; Li, B.; Qin, R.; Zhao, H.; Ren, X.; Su, Z. *Nanotechnology* **2010**, *21*, 285701.
(40) Papkovsky, D. B.; Dmitriev, R. I. *Chem. Soc. Rev.* **2013**, *42*, 8700.
(41) Weissleder, R. *Nat. Biotechnol.* **2001**, *19*, 316.
(42) Tian, G.; Gu, Z.; Zhou, L.; Yin, W.; Liu, X.; Yan, L.; Jin, S.; Ren, W.; Xing, G.; Li, S.; Zhao, Y. *Adv. Mater.* **2012**, *24*, 1226.
(43) Qian, H. S.; Zhang, Y. *Langmuir* **2008**, *24*, 12123.
(44) Chen, F.; Bu, W.; Zhang, S.; Liu, J.; Fan, W.; Zhou, L.; Peng, W.; Shi, J. *Adv. Funct. Mater.* **2013**, *23*, 298.
(45) Pan, L.; He, Q.; Liu, J.; Chen, Y.; Ma, M.; Zhang, L.; Shi, J. *J. Am. Chem. Soc.* **2012**, *134*, 5722.
(46) Fan, W.; Shen, B.; Bu, W.; Chen, F.; Zhao, K.; Zhang, S.; Zhou, L.; Peng, W.; Xiao, Q.; Xing, H.; Liu, J.; Ni, D.; He, Q.; Shi, J. *J. Am. Chem. Soc.* **2013**, *135*, 6494.
(47) Tu, D.; Liu, L.; Ju, Q.; Liu, Y.; Zhu, H.; Li, R.; Chen, X. *Angew. Chem., Int. Ed.* **2011**, *50*, 6306.
(48) Ju, Q.; Tu, D.; Liu, Y.; Li, R.; Zhu, H.; Chen, J.; Chen, Z.; Huang, M.; Chen, X. *J. Am. Chem. Soc.* **2011**, *134*, 1323.
(49) Boyer, J.-C.; van Veggel, F. C. J. M. *Nanoscale* **2010**, *2*, 1417.
(50) Michalet, X.; Pinaud, F. F.; Bentolila, L. A.; Tsay, J. M.; Doose, S.; Li, J. J.; Sundaresan, G.; Wu, A. M.; Gambhir, S. S.; Weiss, S. *Science* **2005**, *307*, 538.
(51) Lee, J. E.; Lee, N.; Kim, H.; Kim, J.; Choi, S. H.; Kim, J. H.; Kim, T.; Song, I. C.; Park, S. P.; Moon, W. K.; Hyeon, T. *J. Am. Chem. Soc.* **2010**, *132*, 552.
(52) Gorris, H. H.; Ali, R.; Saleh, S. M.; Wolfbeis, O. S. *Adv. Mater.* **2011**, *23*, 1652.
(53) Zhang, H.; Sun, Y.; Ye, K.; Zhang, P.; Wang, Y. *J. Mater. Chem.* **2005**, *15*, 3181.
(54) Vordermark, D.; Brown, J. M. *J. Radiat. Oncol.* **2003**, *56*, 1184.
(55) Smith, A. R.; Shenvi, S. V.; Widlansky, M.; Suh, J. H.; Hagen, T. M. *Curr. Med. Chem.* **2004**, *11*, 1135.
(56) Jou, C. J.; Spitzer, K. W.; Tristani-Firouzi, M. *Cell. Physiol. Biochem.* **2010**, *25*, 419.